To appear in the Publications of the Astronomical Society of the Pacific
Preprint typeset using LaTeX style emulateapj v. 03/07/07

PHOTOMETRY USING THE INFRARED ARRAY CAMERA ON THE SPITZER SPACE TELESCOPE

Joseph L. Hora[1], Sean Carey[2], Jason Surace[2], Massimo Marengo[1], Patrick Lowrance[2], William J. Glaccum[2], Mark Lacy[2], William T. Reach[2], William F. Hoffmann[3], Pauline Barmby[4], S. P. Willner[1], Giovanni G. Fazio[1], S. Thomas Megeath[5], Lori E. Allen[1], Bidushi Bhattacharya[6], Manuel Quijada[7]

To appear in the Publications of the Astronomical Society of the Pacific

ABSTRACT

We present several corrections for point source photometry to be applied to data from the Infrared Array Camera (IRAC) on the Spitzer Space Telescope. These corrections are necessary because of characteristics of the IRAC arrays and optics and the way the instrument is calibrated in-flight. When these corrections are applied, it is possible to achieve a ∼2% relative photometric accuracy for sources of adequate signal to noise in an IRAC image.

Subject headings: infrared, instrumentation, calibration, IRAC, Spitzer Space Telescope

1. INTRODUCTION

The Infrared Array Camera (IRAC) was built at the NASA Goddard Space Flight Center under the direction of a team led by Giovanni Fazio at the Smithsonian Astrophysical Observatory (Fazio et al. 2004). IRAC is the mid-infrared camera on the Spitzer Space Telescope (Werner et al. 2004), with four arrays, or "channels", simultaneously taking data in two separate fields of view. The four channels are referred to in this paper with their standard labels of 3.6, 4.5, 5.8, and 8.0 μm for channels 1, 2, 3, 4, respectively, although as described by the IRAC documentation[8] and by Fazio et al. (2004); Reach et al. (2005) the nominal wavelengths differ from these labels. The absolute calibration of the camera was performed in flight by comparison to a set of stars that had been selected and characterized before launch (Megeath et al. 2003; Cohen et al. 2003). Reach et al. (2005) presented the IRAC in-flight calibration results, including the observing strategy, the predictions and measurements, and an assessment of the calibration accuracy and stability of the instrument and the pipeline-processed data provided by the Spitzer Science Center (SSC) to observers.

There are several characteristics of the IRAC instrument that affect the accuracy of the photometry obtained from the images. The effects considered in this paper are:

1. The IRAC science pipeline generates images in units of surface brightness, but because of distortion, the pixels do not subtend constant solid angle. This causes errors in point source photometry that vary over the field of view (FOV) in each channel.

2. The IRAC spectral response varies over the field of view, and therefore the color corrections are field dependent.

3. The electron rates in the 3.6 μm and 4.5 μm channels depend slightly on pixel phase (the position of the star relative to the nearest pixel center). The pipeline calibration factors are correct on average, as is appropriate for sources observed multiple times at multiple dither positions. For the most precise photometry, however, pixel phase should be taken into account.

4. A correction must be applied for the size of the aperture and background region used in aperture photometry, if different from that used by Reach et al. (2005) to derive the calibration from standard stars.

The corrections described in this paper should be applied to the photometry in a manner consistent with those applied by Reach et al. (2005) (which includes using the centroiding technique and the aperture and annulus background sizes described by Reach et al., applying the point source gain correction described in Section 2.2 below, and the pixel phase correction described in Section 3 below), in order for the absolute calibration to remain valid and to achieve <2% photometric accuracy reported.

2. FIELD-OF-VIEW (FOV) DEPENDENT EFFECTS

A portion of the IRAC optical layout is shown in Figure 1, and the details are described by Fazio et al. (2004). This figure shows the relationship between the channels – the two separate fields of view are shared by pairs of channels (channels 1 & 3 and channels 2 & 4). Each pair shares the same doublet lens and is divided at the beamsplitter where the short wavelength light is reflected and long wavelength transmitted. In both channels, the light then passes through filters before entering the detector arrays at an angle that depends on the position in the field of view. The tilted elements and the variable angle of incidence on the filters and array causes some of the effects on the IRAC photometry described below.

Electronic address: jhora@cfa.harvard.edu
[1] Harvard-Smithsonian Center for Astrophysics, 60 Garden Street, MS-65, Cambridge, MA 02138
[2] *Spitzer* Science Center, MS 220-6, California Institute of Technology, Pasadena, CA 91125
[3] Steward Observatory, Univ. of Arizona, Tucson, AZ 85721
[4] Department of Physics & Astronomy, University of Western Ontario, 1151 Richmond St, London, ON N6A 3K7, CANADA
[5] Ritter Observatory, mail drop 113, The University of Toledo, 2801 West Bancroft Street, Toledo, Ohio 43606
[6] NASA/Herschel Science Center, California Institute of Technology, Pasadena, CA 91125
[7] Goddard Space Flight Center, Optics Branch, Code 551, Greenbelt, MD 20771
[8] http://ssc.spitzer.caltech.edu/irac/

2.1. *Distortion and Pixel Area*

The IRAC images have distortion in each channel due to its optical design, resulting in a pixel displacement of ∼2 pixels or less in the corners of the array relative to a regularly-spaced grid aligned with the central pixel (Fazio et al. 2004). The distortion also causes the pixel area to vary slightly over the FOV. The distortion was measured using data taken during In-Orbit Checkout (IOC) period shortly after launch. The distortion can be fit by a quadratic model, which is incorporated into the BCD image headers (Shupe et al. 2005). The change in pixel area over the FOV was estimated by calculating the determinant of the Jacobian of the transformation to the distorted coordinate systems (Sparks et al. 2003). The results are shown in Figure 2. The total ranges of the pixel area changes are 2.5%, 3.2%, 2.4%, and 3.8% for channels 1-4, respectively.

2.2. *Point Source Gain Correction*

The pipeline gain or "flat" correction is determined from observations of the zodiacal background (zodi) emission. Regions of high and low zodi background (near the ecliptic plane and poles, respectively) are observed during an IRAC campaign. The flat image in each band is obtained by rejecting point sources in the dithered frames and differencing the high and low zodi images. The illumination by the zodi is assumed to be uniform over the FOV, so dividing each science image by a normalized version of the flat corrects most of the pixel-to-pixel gain variations that exist in the arrays. The flat correction has been found not to vary over time during the mission within the measurement noise, so data from the whole Spitzer mission have been combined into a "superflat" which is used to correct the data for the entire mission. The SSC will soon reprocess all of the IRAC data with the S18 pipeline, which will use the superflat constructed from the first four years of Spitzer operation.

The flat correction works very well for extended sources with colors similar to the zodi. The changes in pixel area over the FOV due to the geometric distortion are part of the flat, as are the effective wavelength variations, and the BCD are calibrated to units of MJy/sr. In addition, the spectrum of the zodi is quite different than that of a typical star (Figure 3), so essentially the opposite correction for effective wavelength is applied by the flat to data from normal stars. Furthermore, scattered light from extended emission outside of the FOV could affect the flat measurement near the array edges, and light or charge spreading within the array could cause differences between extended and point source photometry. All of these effects and possibly others lead to a variation in the photometry of a point source at different locations on the array. We can use the photometry of a star at many points on the array to derive a correction to apply to remove the variation.

2.2.1. *Data and Analysis*

We derived the point source gain correction from characterization data taken during IOC. The observations were taken after telescope cooldown and final focus adjustment. A standard star (BD+67 1044 = SAO 17718) was observed on a 5x5 grid (a square grid with equal spacings of roughly 50 pixels) across the arrays using Astronomical Observing Requests (AORs) ADS/Sa.Spitzer#0006946816 and ADS/Sa.Spitzer#0006946560. This is a K2 star that had the brightness in the IRAC bands (magnitudes of 6.29, 6.43, 6.39, and 6.33 in channels 1-4, respectively) such that with relatively short frame times (0.4 sec for channels 1 and 2, and 2 sec for channels 3 and 4) the peak pixel could be kept near the middle of the linear range of the detectors and a high S/N measurement of the focus across the FOV could be performed. The short frame times also minimized the number of cosmic rays in the image. At each of the positions of the 5x5 grid, a set of 12 small dithers was performed to minimize the effects of bad pixels or any pixel gain map problems.

From each image, the stellar flux was extracted using the `phot` command in IRAF[9]. A radius of 10 IRAC pixels was used. In each channel, the photometry varies systematically across the FOV. The variations can be fit by a quadratic surface across the arrays, a different one for each IRAC channel. The point source photometry correction factor F_{psp} was found by fitting the function

$$F_{psp}(x,y) = A + B(x-128) + C(y-128) + D(x-128)(y-128) + E(x-128)^2 + F(y-128)^2 \quad (1)$$

where x and y are the pixel coordinates in the BCD frame, and the centers of the pixels run from 1 to 256 in both axes. The convention used by Reach et al. (2005) for this correction in the absolute calibration was to define it relative to pixel (128,128). The polynomial coefficients of the fit are given in Table 1. The fit was performed relative to pixel (128,128), and then the array of correction values was normalized so that the median value of the correction factor over the array is 1. In the case of AORs designed to obtain photometry for a source using a small dither pattern near the center of the array, the correction is near 1.0 in all channels. A cubic fit did not improve the quality of the correction significantly. The fitted surfaces are shown in Figure 4, and the coefficients are listed in Table 1. Correction images that can be applied to IRAC data are supplied on the SSC website[10]. To correct the data, $F_{corr}(x,y) = F_{psp}(x,y) \times F_{measured}$.

In channels 1 and 2, the pattern is "bowl"-shaped, with the uncorrected photometry having the smallest value near the center of the field. For channels 3 and 4, the pattern is dominated by a gradient mostly left-right across the images with opposite signs. The maximum ranges (maximum-minimum correction values) are 4.7%, 5.9%, 13%, and 9% for channels 1-4, respectively. Since the extreme values are at the edges or corners of the arrays, the errors for uncorrected stars closer to the centers of the arrays are much smaller. For example, for objects in the central 128×128 pixel area, the range of corrections are 1.6%, 1.9%, 5.6%, and 4.0%.

Because of the way this correction was derived, it corrects for several of the point source gain errors at once. These include the pixel area difference over the FOV, the changing effective wavelength over the FOV (see section below), and any extended/point source illumination differences. Therefore, the correction is only strictly true

[9] IRAF is distributed by the National Optical Astronomy Observatory, which is operated by the Association of Universities for Research in Astronomy (AURA) under cooperative agreement with the National Science Foundation.

[10] http://ssc.spitzer.caltech.edu/irac/locationcolor/

for stars of the same spectral type as the standard used in these observations. However, in practice the color term of the correction is relatively smaller than the other effects, so the photometry is in general improved when the correction is applied to all point sources.

2.3. *Effective Wavelength Variations over the Field of View*

As a consequence of the wide-field and compact optical design of the cameras, the light at each point of the FOVs passes through the filters at a different average angle, as shown in Figure 1. In addition, the filters are tilted with respect to the optical axis in order to minimize abberations introduced by other optical elements and the off-axis design. The range in angles as a function of position results in a change in effective wavelength over the FOV. The filters were designed to have the desired nominal wavelength and bandpass for the center of the field, given the average filter tilt for the position as specified in the optical design. In addition to the filters, the transmission of the beamsplitters produces angle-dependent reflection variations in channels 1 and 2, and transmission variations in channels 3 and 4. The primary effect is a change in the total transmission or reflection over the band as a function of angle at the beamsplitter. The design of the filters and beamsplitters and the measurements of their transmission and reflectance is detailed by Quijada et al. (2004).

Based on the Quijada et al. (2004) results, we have constructed models of the instrument transmission for each pixel of the four channels. The angles of transmission through the filter and transmission or reflection of the beamsplitter were determined for each pixel, and the total relative system response (RSR) was calculated. This also includes the assumed telescope transmission and the detector quantum efficiency. Then, for a source with a spectrum significantly different than that of the standard stars, the color correction $K_{i,j}$ can be calculated for an object at a particular location in an IRAC frame as described by Reach et al. (2005), where the color correction is defined as:

$$K_{i,j} \equiv \frac{\int (F_\nu/F_{\nu_0}) (\nu/\nu_0)^{-1} R_{i,j} d\nu}{\int (\nu/\nu_0)^{-2} R_{i,j} d\nu}. \quad (2)$$

where F_ν is the source spectrum, F_{ν_0} is the reference spectrum (assumed to be $\nu F_\nu = constant$), $R_{i,j}$ is the instrumental response as a function of frequency at array location (*i,j*), and ν_0 is the nominal frequency.

To illustrate the changes in transmission across the FOV, we have calculated the nominal wavelength at each pixel for each channel, as described by Fazio et al. (2004) for the original instrument response curves. The nominal wavelength was calculated using the following expression at each pixel, integrated over the bandpass:

$$\lambda_0 = \frac{\int R d\lambda}{\int \lambda^{-1} R d\lambda}. \quad (3)$$

Figure 5 shows the variation of the nominal wavelength across the FOV for each of the channels. The nominal wavelength varies from 3.5406 to 3.5512 μm for channel 1, 4.4680 to 4.4949 μm for channel 2, 5.6718 to 5.7458 μm for channel 3, and 7.6212 to 7.8929 μm for channel 4. The dominant change over the fields is a shift of the entire transmission pattern, although there are some small changes in the details of the relative response curves as one moves around the FOV, and in Channels 3 and 4 there is a significant difference in the average transmission over the field, mainly due to variations in the beamsplitter transmission as noted by Quijada et al. (2004). To first order this transmission change should be compensated for by the flat correction in the BCD pipeline.

By applying the photometry correction described in section 2.2 above, one is also implicitly applying a correction for the wavelength variation effect because the correction was derived based on standard stars. Therefore, if a source of interest has a spectrum similar to the standard star, no further wavelength correction is necessary. If the source spectrum is different from the standard, the correction for the standard star must be backed out before the correction is applied to the data for the specific source of interest.

Based on the instrument response curves for the individual pixels, we also calculated average response curves for the entire array and for the subarray. These are shown in Figures 6 – 9. Each figure shows the transmission curves averaged over the entire array, the subarray region, and also plots of the pixels with extremes in nominal wavelength for that channel. These data are available on the SSC website[11], including the full 3-d datacube with the instrument response for each pixel for all channels.

3. INTRA-PIXEL GAIN EFFECTS

The optical point spread function (PSF) is slightly undersampled by the IRAC pixel scale. The optical model predicted image FWHM sizes of 1.6, 1.6, 1.8, and 1.9 arcsec for channels 1-4 respectively, with a pixel size of 1.2 arcsec in all channels. The small size of the PSF causes the IRAC photometry to be sensitive to intra-pixel gain variations, due to variations of the quantum efficiency across a pixel area or gaps between pixels.

The intra-pixel gain effects were investigated by examining photometry of stars at many different positions on the array. The photometry was extracted and the point source gain correction, as described in Section 2.2 above, was applied. Then for each measurement, the photometry relative to the median value for that star for all positions was plotted against the distance from the source centroid to the center of the nearest pixel. The results are shown in Figure 10. For channels 1 and 2, there is a correlation between the source location relative to the pixel center (or "pixel phase") and the extracted photometry. As expected, the magnitude of this correlation is dependent on the wavelength (or size of the PSF) – the effect is greatest in channel 1, less in channel 2, and not detected in channels 3 and 4.

If the correction is defined to be unity for the median location of a source in a pixel (for randomly placed sources this location is $1/\sqrt{2\pi}$ pixels from the center) the correction is given by

$$f_{IPG} = 1 + A(1/\sqrt{2\pi} - p) \quad (4)$$

[11] http://ssc.spitzer.caltech.edu/irac

where p is the distance (in pixels) from the source centroid to the nearest center ($0 \leq p \leq \sqrt{2}/2$). For channel 1, $A = 0.0535$, and for channel 2, $A = 0.0309$.

Reach et al. (2005) performed a correction only for channel 1, where the effect is the largest. The channel 1 calibration stars tended on average to fall closer to the centers of their pixels than a random distribution, due to the difficulty in estimating the true centroid of the flux distribution. The median correction $\langle f_{phase} \rangle = 1.0\%$.

This form of the pixel phase correction uses only one parameter, the radial distance of the centroid from the center of the pixel. Since the detectors are square, a better parameterization of the effect would be based on the x,y distance from the pixel center and also perhaps include a model of the pixel response across the width of the pixel. We have derived such a correction using a simple model of the pixel response (Hoffmann 2005), and Mighell (2007, 2008) has incorporated this into his photometry technique and demonstrated an improved correction. Variations in the detailed response of each individual pixel may present the ultimate limit of how well the pixel phase can be corrected in a set of observations. Probably the most detailed information is available for the pixels where the transiting planets have been observed, since this usually involves uninterrupted periods of repeated observations of the same source without dithering. There is some periodic spacecraft pointing drift that causes the source to move back and forth across neighboring pixels. For example, Charboneau et al. (2005) detected the pixel phase variations in their 4.5 μm observations of the transiting planet which they were able to reduce the residual RMS of their time series to 0.27%.

4. APPLYING THE PHOTOMETRY CORRECTIONS

4.1. *Correcting photometry extracted from the BCD*

In the case where the point source is sampled at sufficient signal to noise in a single exposure, the most straightforward approach is to apply corrections to the BCD since the corrections are based on position in the FOV of each frame. For a point source in the frame, after it is extracted using photometry software, the PSF flat field correction is applied based on the centroid of the object. For channels 1 and 2, the intra-pixel gain correction can also be applied, based on the pixel phase. If a color correction is necessary, then the correction is calculated based on the source spectrum and the PSF position and applied to the photometry.

Figure 11 shows an example of a test case where the pixel phase and point source gain corrections were applied. The top plot shows the relative Channel 1 photometry of stars as a function of distance from the center of the photometric correction pattern in Figure 4. A linear fit to the data illustrates the trend of lower photometry near the center of the pattern. The second plot shows the same data after the gain corrections have been applied. The linear fit to the relative photometry now shows no trend with position on the array, and the scatter for many of the positions is noticeably lower. Figure 12 shows the effect of the phase correction on the photometry. For stars of several fluences, the standard deviation of the photometry at a particular point on the array was calculated from the available measurements. Also shown are the results from the same data after the intrapixel gain correction was applied. The reduction in the scatter of the photometry was about 0.5% for the stars examined.

4.2. *Correcting photometry extracted from mosaics*

Correcting photometry extracted from mosaics is more complicated because the image at any point source location is the combination of images at several different FOV positions in the individual frames. The pixels contain some mixture of extended and point source emission. Therefore if one applies the correction before mosaicing, the correction is wrongly applied to the extended emission, and that will create artifacts in the images.

One possible way to apply the point source gain correction to mosaics is to extract the photometry from the uncorrected mosaic and also to calculate a separate correction map. The correction map is calculated by successively offsetting the BCD correction image to the same locations as the science images and calculating the mean corrections at each location in the final mosaic. The BCD correction image, however, includes the correction for the change in pixel area over the array, and the mosaics have been reprojected to a constant pixel area. Therefore we have to divide out the pixel area normalization from the BCD correction image before we use it to make the mosaic correction map.

An example of such a correction map for a mapping AOR with dithers is shown in Figure 13. For each source, one would need to determine its pixel coordinates and use the value at the same location in the correction mosaic to correct the photometry. This approach will work in cases where either the target is of high surface brightness relative to the local extended emission, including the zodi, or the extended emission has a spectrum similar to the zodi emission. The wavelength-dependent part of the correction depends on the spectral slope of the sum of the extended and pointlike emission (i.e. what actually arrived at the detector), not the spectral slope of the point source alone. If the local extended-source spectrum differs from the zodi, the extended emission is also in need of correction, and so the method will have problems in proportion to the strength of the extended emission.

The correction mosaics themselves will have seams all through them as seen in Figure 13, and it isn't obvious for an object whose photometry is derived from many pixels just how to derive a single correction factor applicable to the catalog entry except by duplicating the extraction procedure. The correction would be even more difficult to derive for PSF fitting. A PSF-weighted average of the pixels in the correction mosaic might closely approximate the correction value for a particular position in the mosaic.

For a data set such as an extragalactic survey like SWIRE that has a relatively uniform background and few bright, extended emission sources, the data can be split into a nearly constant "background" and residual "object" components, and the corrections in image space applied to the "object image". Then the zodi-flattened (zodi-colored) background can be put back in. The resulting mosaics would be seamless and fully calibrated for either point sources or extended emission. However, this technique is possible only where the background is uniform and has a color similar to the zodi emission.

A fully generic implementation, which is under development at the SSC, will involve pixel-wise corrections that take into account the pixel colors and thus be correct for both point sources and extended emission.

4.3. *Aperture corrections*

The IRAC calibration described by Reach et al. (2005) used a 10 pixel aperture and an aperture with an inner radius of 12 pixels and outer radius of 20 pixels. This is appropriate for measuring standard stars since they were chosen to be extremely bright relative to background objects within this distance on the sky. The aperture contains a large fraction of the total flux from the object, but is small enough so that it does not extend off the array when extracting the photometry from BCDs where the star is offset at different positions on the array. However, for many other applications where one is extracting sources in crowded fields or where there is significant extended emission near the source, a smaller aperture is likely to produce more accurate photometry. In order to calibrate the photometry using aperture sizes different from that of the standard star observations, one must perform an extraction of the same star(s) using the different parameters, and a correction factor can then be determined. This analysis was performed based on observations of a standard star at many different positions on the array. The procedure `aper` in IDLPHOT was used to extract the photometry from the BCD, and the average corrections were determined. The results are reported in the IRAC Data Handbook[12] (IDH; see Table 5.7 of the Handbook). Note that for extracting photometry from the BCD, there might be a position dependence due to the distortion, especially for small apertures. This has not been taken into account in the IDH where the average value for all positions with the same pixel aperture dimensions are reported.

The aperture correction values in the IDH were determined from the BCD of a star with high S/N observations and many positions on the array. Many observers instead extract photometry from mosaics for which the number of dithers at each position and the reprojected pixel size is different from the instrumental pixels. The data set and the choices one makes in the reduction parameters can make a difference in the aperture photometry corrections. In order to illustrate this, we measured the aperture corrections for two different datasets using a few different mosaic parameters. The datasets that were used were an AOR from the Extragalactic First Look Survey (FLS; Lacy et al. 2005, - ADS/Sa.Spitzer#0003863296), and a mosaic made from the SAGE data (Meixner et al. 2006) contained in an area of 0.7x0.7 deg, centered on 77.5d R. A., -65.166667 Dec. (J2000.0). The FLS AOR used a mapping pattern with 5x100s dithers at each map point. The SAGE data were taken with a coverage of 2x12s HDR frames in two separate epochs separated by approximately 3 months, so at each position the depth of coverage is at least 4 frames with two different rotation angles roughly 90° apart. The location of the SAGE mosaic was chosen to be in a region of good coverage in a corner of the field, far from the dense LMC stellar distribution and any extended emission.

The data for each survey field were mosaicked to a pixel scale of 0.″6/pixel using IRACproc (Schuster et al. 2006), which is based on the mopex software produced by the SSC (Makovoz et al. 2006). We also used the post-BCD product generated by the SSC for the FLS data, which is at a scale of 1.″2/pixel. For each mosaic, we used the `daofind` and `phot` tasks in IRAF to find and extract photometry for the sources in the field. We used only those sources with a S/N>100, and also used a minimum flux cutoff to exclude the fainter sources. The same sources were extracted using the same range of apertures and background annulus sizes that were used to produce the table of corrections in the IDH. The ratio of fluxes relative to the photometry using a 10 pixel aperture with a background annulus range from 10-20 pixels were calculated, and the median ratio was determined for each set of parameters. The estimated uncertainties of the ratios are approximately 0.002, 0.003, 0.007, and 0.008 in channels 1 - 4, respectively. The results are summarized for each channel in Tables 3 - 6.

The first column of each table shows the IDH values for comparison. The values are very similar for channels 3 and 4; the largest variations are in channel 1 and 2. Several effects could influence the correction factors, including the pixel scale of the mosaics (as shown in the FLS 0.6 and PBCD results), differences in mosaic mapping and dithering techniques and depths (compare the LMC 0.6 to the FLS 0.6), and software that was used to extract the photometry (compare the IDH values to all others reported here). For the most accurate aperture correction factors, one should determine the corrections based on the data that one is performing the photometry on, or on a data set taken with a similar observing strategy.

5. CONCLUSIONS

The IRAC camera has FOV-dependent transmission characteristics that affect the measurement of astronomical sources. After correction of these effects for standard stars, Reach et al. (2005) found that the calibration has a relative accuracy of 1.8%, 1.9%, 2.0%, and 2.1% in channels 1 (3.6 μm), 2 (4.5 μm), 3 (5.8 μm), and 4 (8 μm), respectively. To measure fluxes at this level of accuracy requires several photometric corrections: array position dependence (due to changing spectral response and pixel solid angle over the camera of view), pixel phase dependence (due to nonuniform quantum efficiency over a pixel), color correction (due to the different system response integrated over the passband for sources of different color), and aperture correction (due to the fractions of light included within the measurement aperture and lost in the background aperture). The same accuracies are possible for sources with spectra similar to the A-type standards used in the absolute calibration with the array position dependence, pixel phase, and aperture corrections. For sources with spectra different from A stars, a knowledge of the source spectrum is necessary to make the necessary color corrections to achieve the same photometric accuracy.

This work is based on observations made with the Spitzer Space Telescope, which is operated by the Jet Propulsion Laboratory, California Institute of Technology under NASA contract 1407. Support for this work

[12] http://ssc.spitzer.caltech.edu/irac/dh/

was provided by NASA through an award issued by JPL/Caltech.

Facilities: Spitzer (IRAC)

REFERENCES

Charbonneau, D., Allen, L. E., Megeath, S. T., Torres, G., Alonso, R., Brown, T. M., Gilliland, R. L., Latham, D. W., Mandushev, G., O'Donovan, F. T., Sozzetti, A. 2005, ApJ, 626, 523

Cohen M., Megeath, S. T., Hammersley, P. L., Martín-Luis, F., & Stauffer, J. 2003, AJ, 125, 2645

Fazio, G. G. et al. 2004, ApJS, 154, 10

Hoffmann, W. F. 2005, IRAC technical memo IRAC/TM05-028 (Smithsonian Astrophysical Observatory)

Kelsall, T. et al., 1998, ApJ, 508, 44

Lacy, M. et al. 2005, ApJS, 161, 41

Makovoz, D., Roby, T., Khan, I., Booth, H. 2006, in *Advanced Software and Control for Astronomy*, eds. H. Lewis & A. Bridger, Proc. SPIE, 6274, 62740C

Megeath, S.T., Cohen, M., Stauffer, J., Hora, J., Fazio G., Berlind, P., & Calkins, M. 2003, in Proc. "The Calibration Legacy of the ISO Mission", ed. L. Metcalfe, VILSPA, Spain (ESA SP-481), pg.165

Meixner, M. et al. 2006, AJ, 132, 2268

Mighell, K. J. 2007, in *Astronomical Data Analysis Software and Systems XVI*, ASP Conference Series, Vol. 376, eds, R. A. Shaw, F. Hill & D. J. Bell., 405

Mighell, K. J. 2008, PASP, in press

Quijada, M. A., Trout Marx, C., Arendt, R. G., & Moseley, S. H. 2004, Proc. SPIE, 5487, 244

Reach, W. T., Megeath, S. T., Cohen, M., Hora, J., Carey, S., Surace, J., Willner, S. P., Barmby, P., Wilson, G., Glaccum, W., Lowrance, P., Marengo, M., & Fazio, G., 2005, PASP, 117, 978

Schuster, M., Marengo, M., Patten, B. 2006, in *Observatory Operations: Strategies, Processes, and Systems*, eds. D. Silva & R. E. Doxsey, Proc. SPIE, 6270, 627020

Shupe, D. L., Moshir, M., Makovoz, D., Narron, R. 2005, in *Astronomical Data Analysis Software and Systems XIV*, eds. P. L. Shopbell, M. C. Britton, & R. Ebert (San Francisco: ASP), in press

Sparks, W. B., Jedrzejewski, R., Clampin, M., & Bohlin, R. C. 2000, Instrument Science Report ACS 2000-03, http://www.stsci.edu/hst/acs/documents/isrs/isr0003.pdf (AURA)

Werner, M. W. et al. 2004, ApJS, 154, 1

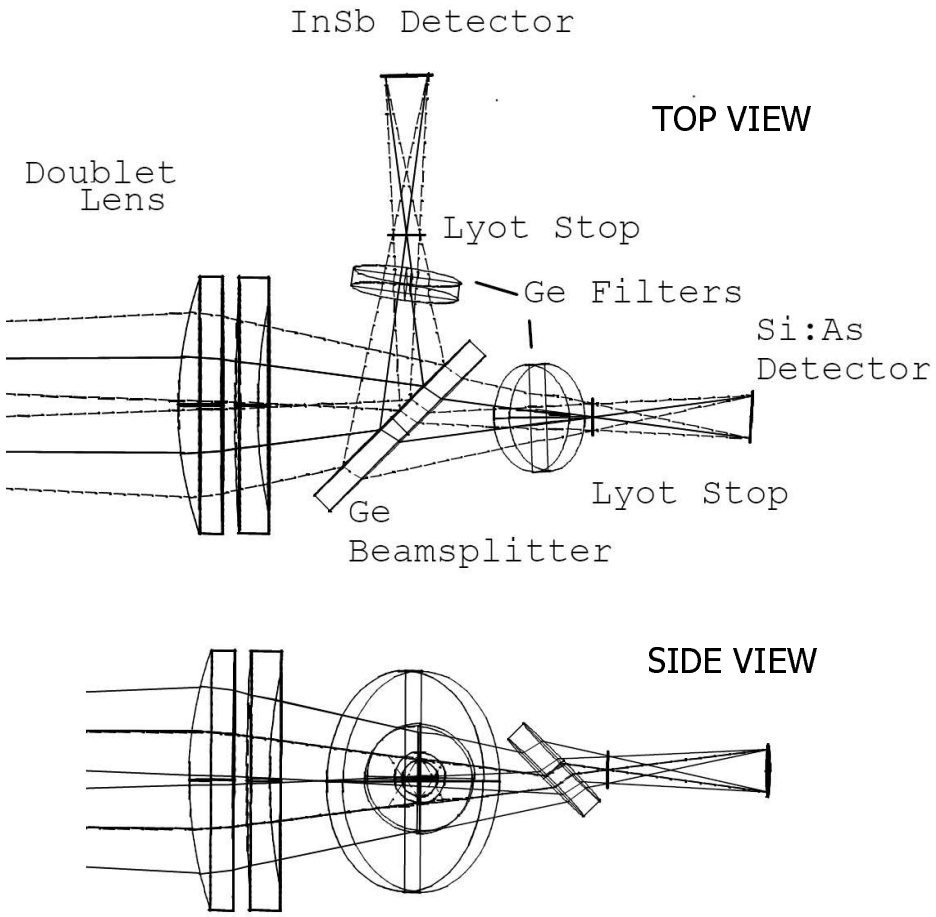

FIG. 1.— The IRAC optical design layout (interior to the camera body), showing the side view and top view. There are two fields viewed simultaneously, with channels 1 and 3 viewing one field and channels 2 and 4 the other. In each pair, the light is reflected from the surface of the beamsplitter and passes through a filter to the InSb detector (channels 1 and 2). The longer wavelength light passes through the beamsplitter and filters to the Si:As detectors (channels 3 and 4). The range of angles of incidence on the filters and beamsplitters depending on position in the field of view is apparent from the rays traced through the system.

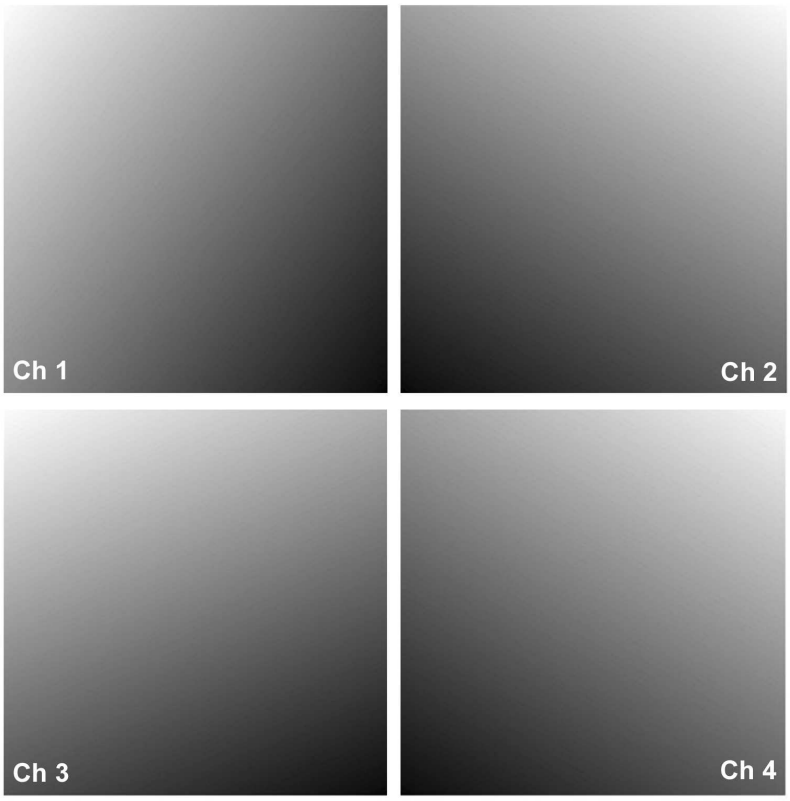

FIG. 2.— Distortion correction images for each of the IRAC channels. Darker regions represent regions where response to a point source has a lower value than in the lighter regions. The full range of variations are 2.5%, 3.2%, 2.4%, and 3.8% for channels 1-4, respectively. The arrays are shown in "BCD orientation", with the first pixel in the FITS file shown in the lower left of each image, with the most rapidly varying index from left to right.

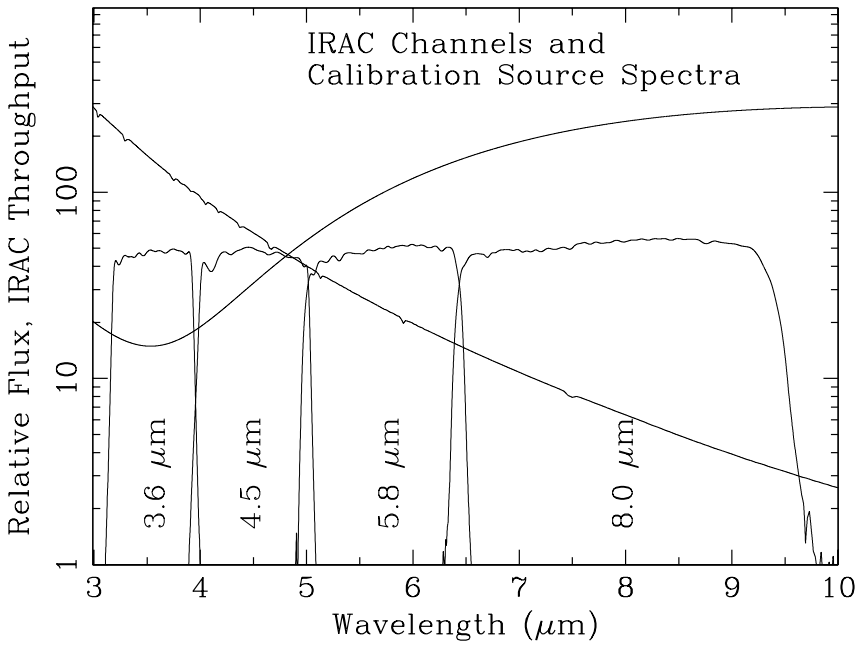

FIG. 3.— The relative band transmissions of the four IRAC channels are shown compared to the spectra of an A0V standard star, and a model of the zodi emission in the ecliptic pole region (Kelsall et al. 1998). The vertical axis is the logarithm of the total instrumental transmission (Fazio et al. 2004), or for the star and zodi it is the logarithm of the flux density (W $cm^{-2}\mu m^{-1}$) scaled to fit on the plot.

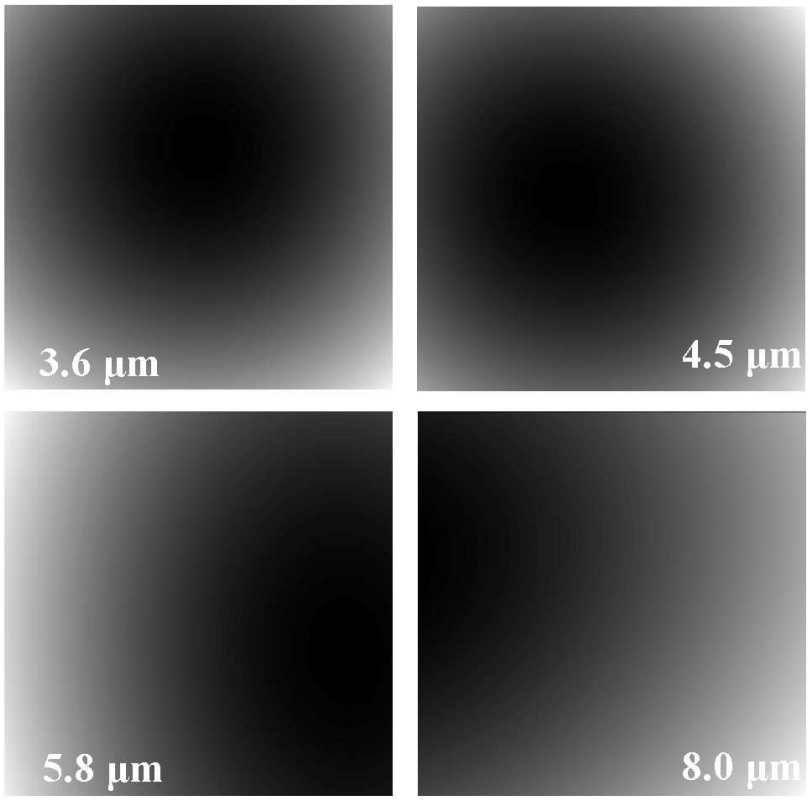

FIG. 4.— The point source photometry correction images for each IRAC band. Darker regions represent regions where the photometry of a point source has a lower value than in the lighter regions. The photometry therefore should be divided by the value given in the images to correct the measurement relative to the center of the array.

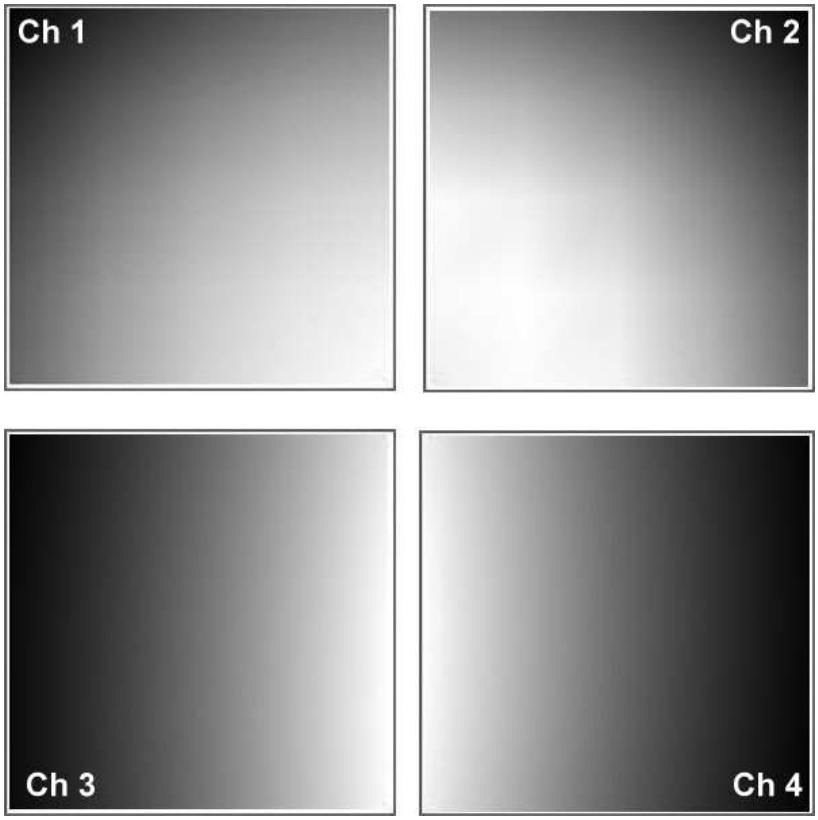

FIG. 5.— Changes to the nominal wavelength over the FOV for each of the IRAC bands. The images are shown in the BCD orientation. Darker areas represent regions of shorter (lower) wavelength. The nominal wavelength varies from 3.5406 to 3.5512 μm for channel 1, 4.4680 to 4.4949 μm for channel 2, 5.6718 to 5.7458 μm for channel 3, and 7.6212 to 7.8929 μm for channel 4.

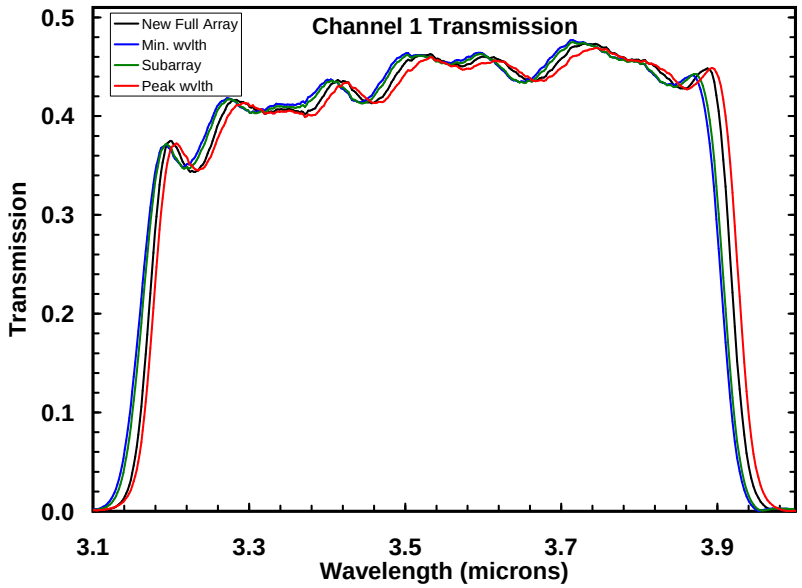

FIG. 6.— The instrument response function for various locations on the array for channel 1 ("3.6 μm"). The full array average is shown in black. The 32×32 subarray response curve is shown in green. The pixel with the lowest nominal wavelength is shown in blue, and the location with the highest wavelength in red.

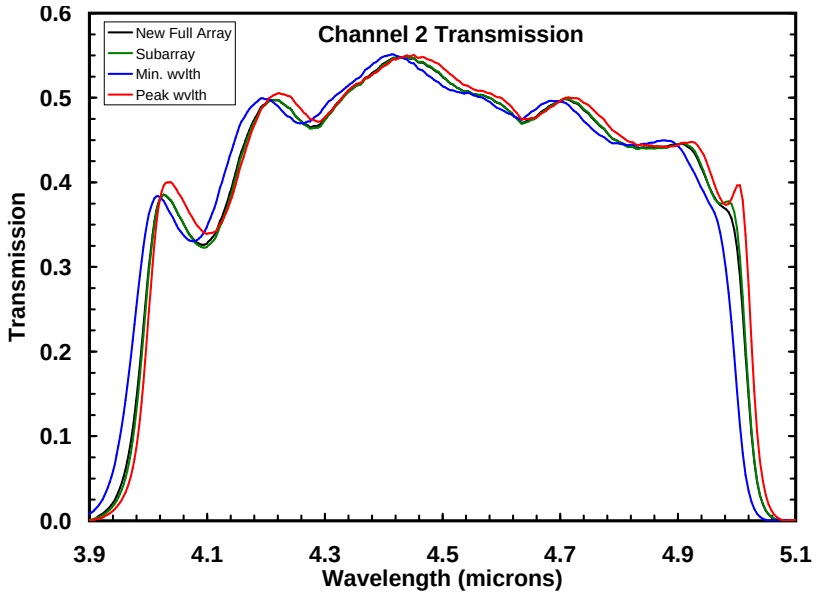

FIG. 7.— The instrument response function for various locations on the array for channel 2 ("4.5 μm"). The full array average is shown in black. The 32×32 subarray response curve is shown in green. The pixel with the lowest nominal wavelength is shown in blue, and the location with the highest wavelength in red.

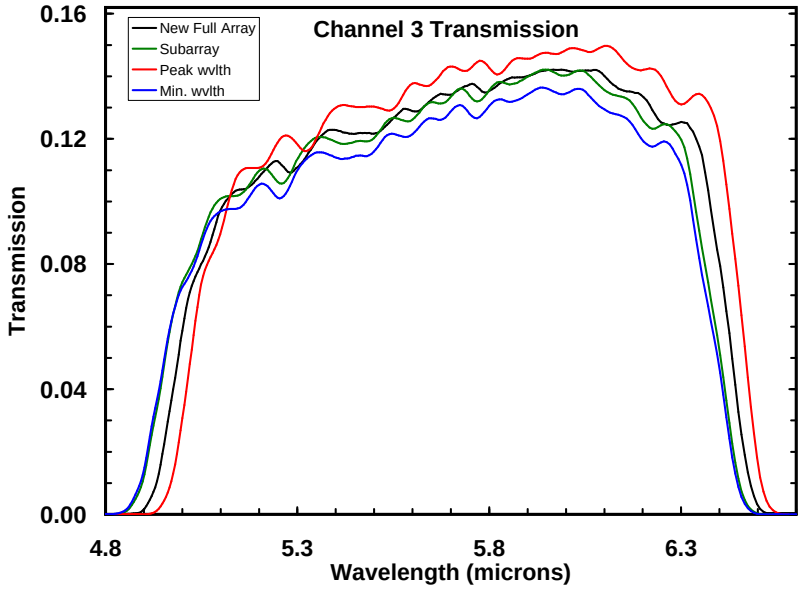

FIG. 8.— The instrument response function for various locations on the array for channel 3 ("5.8 μm"). The full array average is shown in black. The 32×32 subarray response curve is shown in green. The pixel with the lowest nominal wavelength is shown in blue, and the location with the highest wavelength in red.

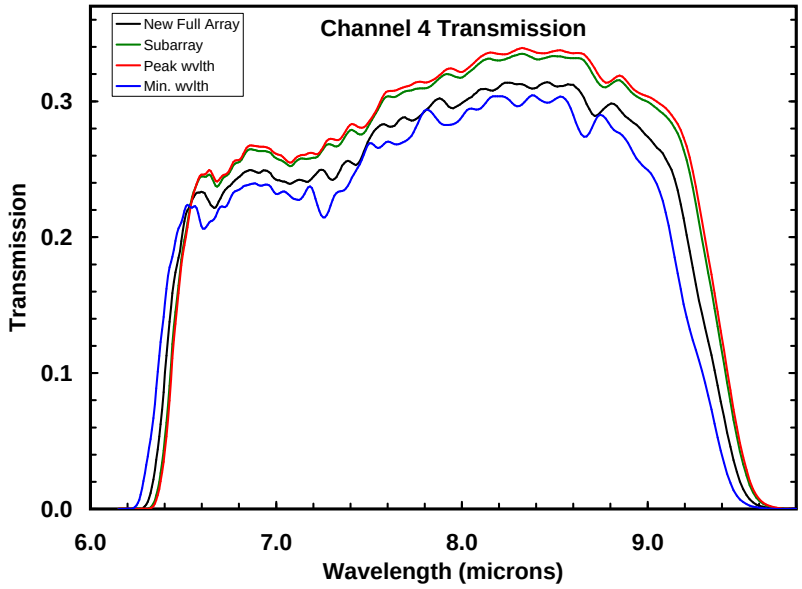

FIG. 9.— The instrument response function for various locations on the array for channel 4 ("8.0 μm"). The full array average is shown in black. The 32×32 subarray response curve is shown in green. The pixel with the lowest nominal wavelength is shown in blue, and the location with the highest wavelength in red.

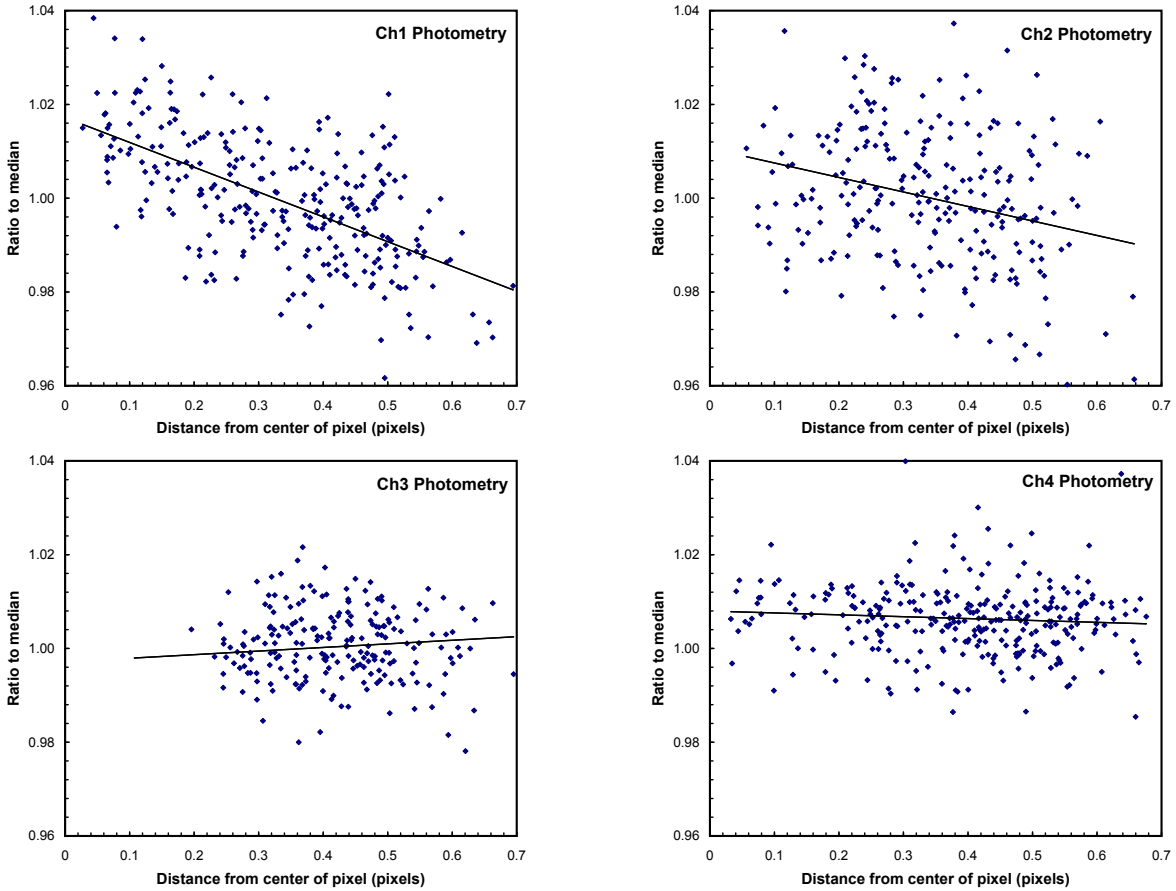

FIG. 10.— Intra-pixel gain effects on the photometry in each channel. The extracted photometry of a source is plotted against the pixel phase. The strongest effect is in the shortest wavelength channel, there is no significant effect detected in channels 3 and 4 for the photometric standard star data examined.

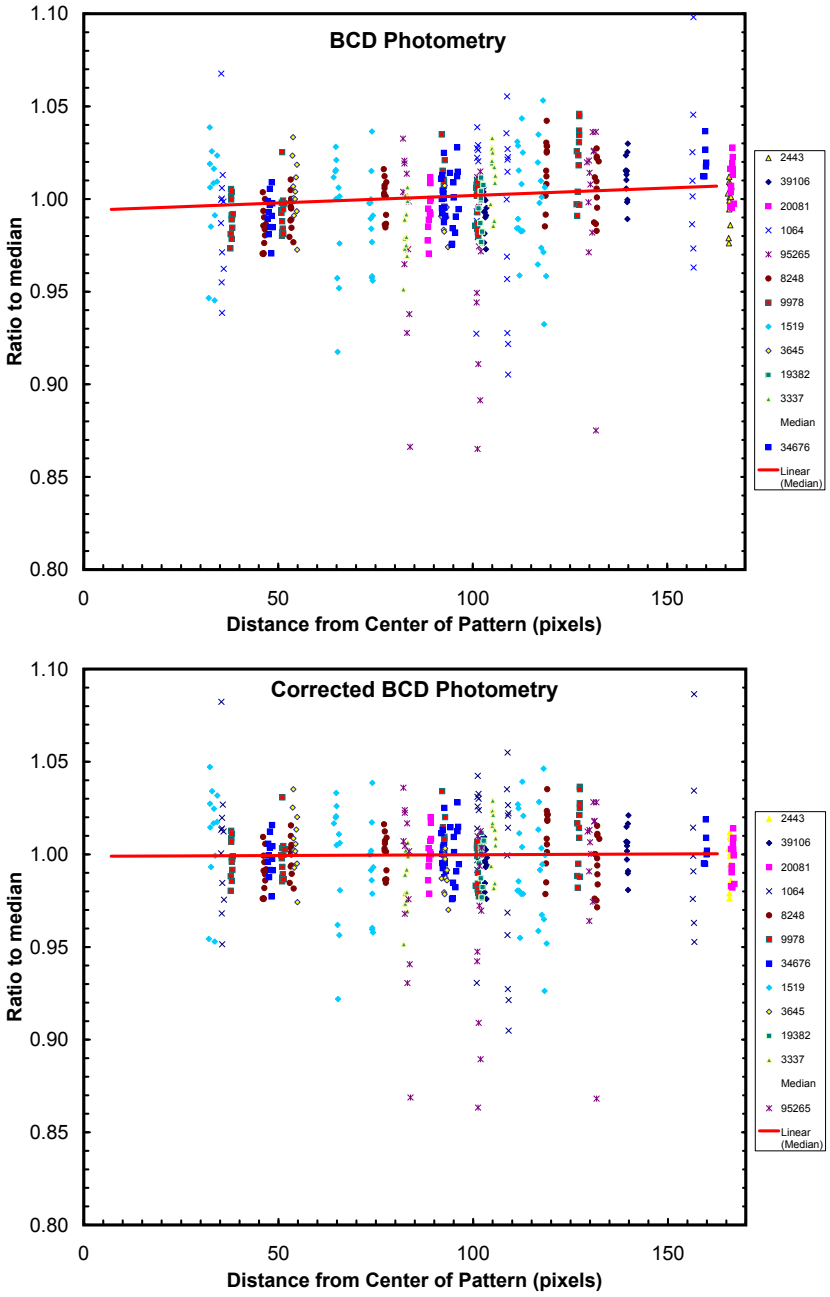

FIG. 11.— The top plot shows the relative photometry of stars in a test field in Channel 1 (the ratio of the measurement to the median value at that array position) as a function of the distance from the center of the photometric correction pattern in Figure 4. Individual stars have unique colors and symbols, several stars have multiple measurements at different array positions. A linear fit to the median values shows the trend of lower values towards the center. The lower plot shows the results after the gain corrections have been applied. The overall trend with array position is removed, and the scatter of individual positions is reduced.

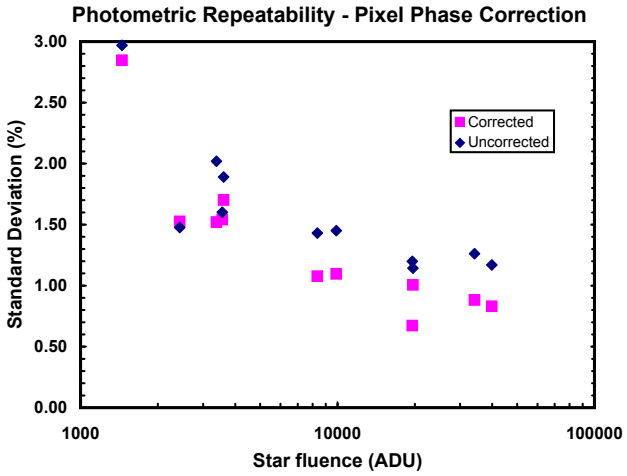

FIG. 12.— The standard deviation of photometry of several stars observed in Channel 1, plotted against the fluence in ADUs. The dark blue points are uncorrected, the magenta points are after the intrapixel gain correction has been applied. The standard deviations are reduced by about 0.5% for most stars.

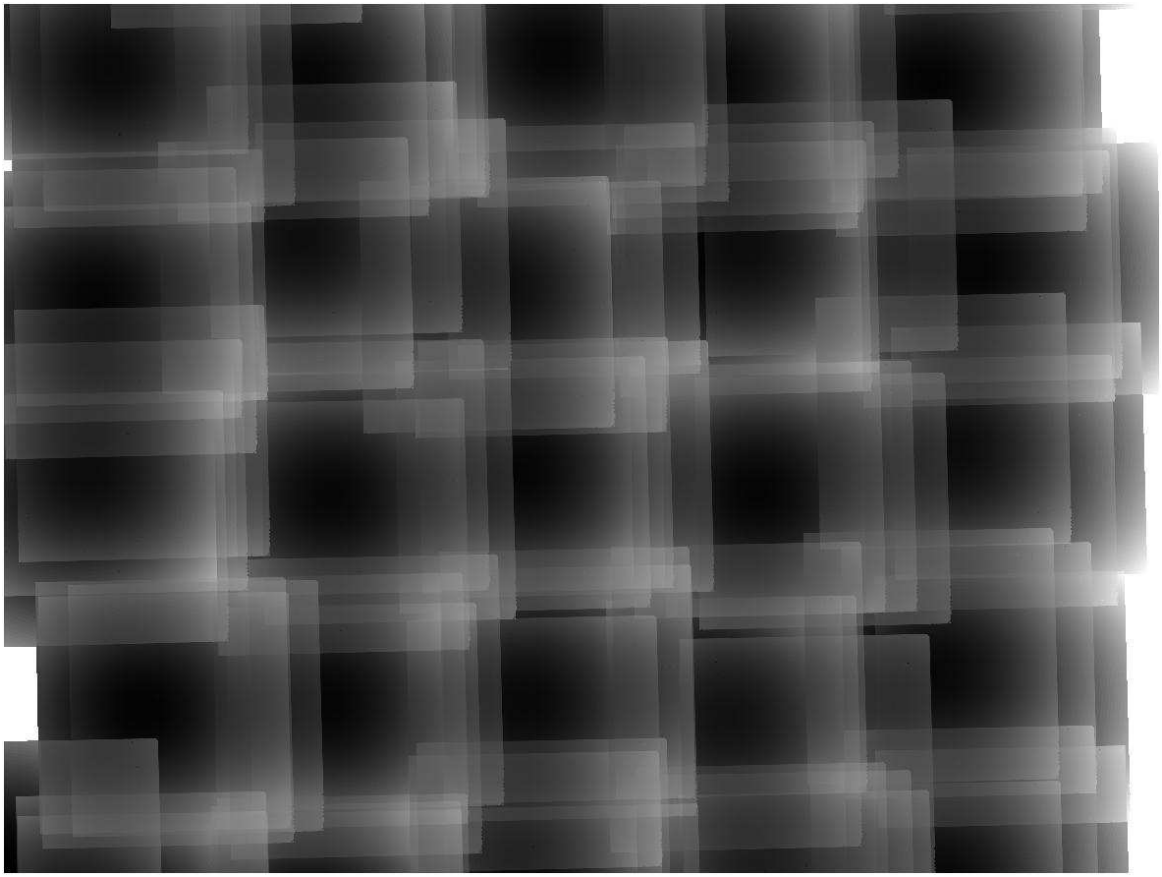

FIG. 13.— Point source photometry correction image for a channel 1 mosaic made from a mapping AOR that used three dithers per map position. The range of correction values is -1.2% (the dark regions) to +3.4% (the ligher areas).

TABLE 1
IRAC Photometry correction fit coefficients.

IRAC Channel	Coefficients[a]					
	A	*B*	*C*	*D*	*E*	*F*
1	1.0114	-3.536E-6	-6.826E-5	-1.618E-8	1.215E-6	1.049E-6
2	1.0138	8.401E-5	3.345E-7	1.885E-7	1.438E-6	1.337E-6
3	1.0055	-3.870E-4	4.600E-5	1.956E-7	2.078E-6	9.970E-7
4	1.0054	2.332E-4	-8.234E-5	-1.881E-7	6.520E-7	9.415E-7

[a]The coefficient labels are defined in equation 2.2.1

TABLE 2
IRAC Channel Transmission Summary

IRAC Channel	Nominal Wavelength (μm)	Central[a] Wavelength (μm)	Bandpass[b] (μm)	Bandpass (percent)	Average[c] Transmission
1	3.544	3.543	0.747	21.1	0.430
2	4.479	4.501	1.018	22.7	0.469
3	5.710	5.711	1.412	24.8	0.125
4	7.844	7.905	2.910	37.0	0.280
Subarray:					
1	3.534	3.538	0.740	20.9	0.426
2	4.489	4.506	1.009	22.5	0.457
3	5.679	5.687	1.383	24.3	0.122
4	7.884	7.912	2.861	36.4	0.289

[a]The central wavelength is defined as the midpoint between the half-power points of the bandpass. The half-power points are defined as being the wavelengths where the transmission is 50transmission.
[b]The bandpass is the distance in wavelength between the half-power points of the transmission.
[c]The average transmission is determined by averaging the transmission between the half-power points of the bandpass.

TABLE 3
Channel 1 Aperture Correction Factors

aperture radius[a]	annulus range	IDH[b]	FLS 0.6[c]	FLS PBCD[d]	LMC 0.6[e]
5	10-20	1.049	1.049	1.057	1.057
5	5-10	1.061	1.057	1.066	1.068
3	10-20	1.112	1.101	1.124	1.128
3	3-7	1.124	1.111	1.138	1.141
2	10-20	1.205	1.167	1.254	1.243
2	2-6	1.213	1.174	1.263	1.251

[a]aperture and annulus ranges are in native pixel units (1.″22).
[b]IRAC Data Handbook values
[c]First Look Survey data, 0.6 arcsec/pixel mosaic
[d]First Look Survey data, 1.2 arcsec/pixel post-BCD mosaic
[e]SAGE LMC data, 0.6 arcsec/pixel mosaic, both epochs

TABLE 4
Channel 2 Aperture Correction Factors

aperture radius[a]	annulus range	IDH[b]	FLS 0.6[c]	FLS PBCD[d]	LMC 0.6[e]
5	10-20	1.050	1.059	1.059	1.063
5	5-10	1.064	1.074	1.074	1.077
3	10-20	1.113	1.124	1.126	1.129
3	3-7	1.127	1.136	1.139	1.141
2	10-20	1.221	1.250	1.266	1.262
2	2-6	1.234	1.263	1.282	1.277

[a]aperture and annulus ranges are in native pixel units (1.″22).
[b]IRAC Data Handbook values
[c]First Look Survey data, 0.6 arcsec/pixel mosaic
[d]First Look Survey data, 1.2 arcsec/pixel post-BCD mosaic
[e]SAGE LMC data, 0.6 arcsec/pixel mosaic, both epochs

TABLE 5
Channel 3 Aperture Correction Factors

aperture radius[a]	annulus range	IDH[b]	FLS 0.6[c]	FLS PBCD[d]	LMC 0.6[e]
5	10-20	1.058	1.055	1.056	1.055
5	5-10	1.067	1.066	1.068	1.064
3	10-20	1.125	1.127	1.135	1.129
3	3-7	1.143	1.148	1.155	1.147
2	10-20	1.363	1.370	1.391	1.386
2	2-6	1.379	1.385	1.408	1.402

[a]aperture and annulus ranges are in native pixel units (1.″22).
[b]IRAC Data Handbook values
[c]First Look Survey data, 0.6 arcsec/pixel mosaic
[d]First Look Survey data, 1.2 arcsec/pixel post-BCD mosaic
[e]SAGE LMC data, 0.6 arcsec/pixel mosaic, both epochs

TABLE 6
Channel 4 Aperture Correction Factors

aperture radius[a]	annulus range	IDH[b]	FLS 0.6[c]	FLS PBCD[d]	LMC 0.6[e]
5	10-20	1.068	1.063	1.065	1.065
5	5-10	1.089	1.082	1.085	1.087
3	10-20	1.218	1.217	1.233	1.234
3	3-7	1.234	1.233	1.249	1.248
2	10-20	1.571	1.569	1.587	1.597
2	2-6	1.584	1.585	1.602	1.609

[a]aperture and annulus ranges are in native pixel units (1.″22).
[b]IRAC Data Handbook values
[c]First Look Survey data, 0.6 arcsec/pixel mosaic
[d]First Look Survey data, 1.2 arcsec/pixel post-BCD mosaic
[e]SAGE LMC data, 0.6 arcsec/pixel mosaic, both epochs